Macromolecules

Article

pubs.acs.org/Macromolecules

Nanoporous Crystalline Templates from Double-Crystalline Block Copolymers by Control of Interactive Confinement

Shih-Hung Huang,[†] You-Wei Huang,[†] Yeo-Wan Chiang,*[,†] Ting-Jui Hsiao,[‡] Yung-Cheng Mao,[‡] Cheng-Hung Chiang,[‡] and Jing-Cherng Tsai[‡]

[†]Department of Materials and Optoelectronic Science, National Sun Yat-Sen University, Kaohsiung 80424, Taiwan

[‡]Department of Chemical Engineering, National Chung Cheng University, Chia-Yi 62142, Taiwan

Supporting Information

ABSTRACT: Single, double, and coincident crystallizations under hard or soft confinement are all carried out using a single type of syndiotactic poly(*p*-methylstyrene)-*block*-poly(L-lactide) (*s*PPMS−PLLA) block copolymers. The single crystallization of *s*PPMS matrix can lead to the disordered arrangement of hexagonally packed PLLA cylinders under soft confinement. In contrast, the lamellar nanostructure remained unchanged regardless of the PLLA crystallization under hard or soft confinement. Crystallization-induced morphological transitions from the confined monosized lamella to the metastable dual-sized lamella and finally to the breakout morphology are evident by transmission electron microscopy and small-angle X-ray scattering. The dual-sized lamella is attributed to the thermodynamically and kinetically controlled nanocrystallite growth templating along the ordered microphase separation. Despite crystalline sequences, the double-crystallized morphologies are determined by the first-crystallized event even though the subsequent crystallization temperature is performed under soft confinement. By the control of interactive confinement, ordered crystalline nanosheets and cylindrical monoliths are obtained, providing a novel means for the fabrication of nanoporous crystalline templates.

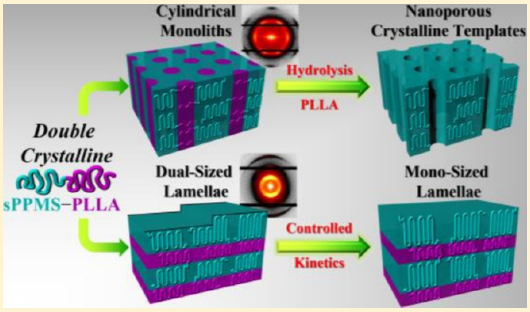

INTRODUCTION

Self-assembly of block copolymers (BCPs) is one of the most convenient ways to generate order structures on nanometer scale. Owing to chemically distinct features between constituted blocks, BCPs having different compositions are able to microphase separate into a variety of periodic nanostructures such as body-centered cubic spheres, hexagonally packed cylinders, gyroids, and lamellae.[1−3] Crystallization in BCPs provides strong driving force to alter the microphase-separated morphologies and their dimensions, which can give rise to a robust crystalline template for practical applications.[4−6] The final morphologies of the crystalline−amorphous BCPs (i.e., semicrystalline BCPs) consisting of one crystallizable block have been demonstrated to be strongly dependent on the order−disorder transition temperature (T_{ODT}), the crystallization temperature (T_c), and the glass transition temperature of the amorphous block (T_g).[7−13] These alterative effects including segregation strength, crystallization, and vitrification result in various crystalline morphologies. In contrast, double-crystalline BCPs possessing two crystallizable blocks give an extra effect of crystallization sequence,[7,11,14−42] leading to numerous crystalline conditions such as one-stage single, two-stage double,[15−29] and coincident crystallization[26,30−41] under soft ($T_c > T_g$) and hard ($T_c < T_g$) confined environment. Unlike the semicrystalline BCP, many studies, including syndiotactic poly(4-methyl-1-pentene)-*block*-poly(L-lactide) (*s*PMP−PLLA),[5] polyethylene-*block*-poly(ethylene oxide) (PE−PEO),[17,22] poly(ε-caprolactone)-*block*-polyethylene (PCL−PE),[18,19] poly(L-lactide)-*block*-poly(ε-caprolactone) (PLLA−PCL),[20,24] poly(L-lactide)-*block*-poly(ethylene oxide) (PLLA−PEO),[25] hydrogenated polynorbornene-*block*-linear polyethylene (hPN−LPE),[26] poly(L-lactide)-*block*-poly(ethylene glycol) (PLLA−PEG),[27] syndiotactic polypropylene-*block*-poly(ε-caprolactone) (*s*PP−PCL),[28] and *it*-poly(propylene oxide)-*block*-poly(ethylene oxide)-*block*-*it*-poly(propylene oxide),[29] reported that the first-crystallized event of the block in double-crystalline BCPs may create a robust environment such that the subsequent-crystallized event is strongly inhibited or confined. Therefore, the final morphologies are mainly determined by the leading crystallization event. Inversely, when the double-crystalline BCP has a shaky first-crystallized texture,[18,19,23] the subsequent-crystallized event is able to overwhelm the leading texture to determine the final morphology, namely, crystallization-sequence dependence. However, various double-crystalline BCPs having different constituted blocks may reveal large differences in the crystal structure, crystal growth orientation, crystalline sequence, and segregation strength, such that the correlation between the final morphology and crystallization in different BCP systems becomes system dependent and uneasy to be compared with each other.

Received: August 8, 2016
Revised: October 17, 2016

ACS Publications © XXXX American Chemical Society

DOI: 10.1021/acs.macromol.6b01725
Macromolecules XXXX, XXX, XXX−XXX

The nanoporous materials especially for ordered amorphous porous nanostructures were frequently employed for nanopatterning platform using PS-based BCPs such as polystyrene-*block*-poly(methyl methacrylate) (PS−PMMA),[43] polystyrene-*block*-polyisoprene (PS−PI),[44] polystyrene-*block*-poly(D,L-lactide) (PS−PLA),[45,46] and polystyrene-*block*-poly(L-lactide) (PS−PLLA).[47] All of them can give the amorphous porous PS nanostructures after the degradation of the other block. This can serve as a nanostructural reactor for the later templating synthesis of organic or inorganic materials. However, the amorphous porous PS nanostructure possesses brittle mechanical property, weak resistance against solvent and heat, limiting the practical applications. In contrast, a nanoporous crystalline template, for instance, nanoporous PE,[48−50] is found to be useful due to the enhanced moisture and solvent resistance. Therefore, the degradable double-crystalline BCP with the well control of interactive crystallization is promising to give an ordered nanoporous crystalline template having improved mechanical property, thermal and solvent resistance, being potential for various practical applications. Also, the inclusive nanocrystallites templating along the order microphase-separated structure under confinement are possible to alter the refractive index contrast so as to exhibit specific optical properties.

Unlike the final morphologies of crystalline BCPs which are strongly dependent upon a type of the constituted blocks, the novel double-crystalline BCP, syndiotactic poly(*p*-methylstyrene)-*block*-poly(L-lactide) (*s*PPMS−PLLA), featuring partial overlapping of the crystallization windows ($T_g \sim T_m^\circ$) for the *s*PPMS and PLLA blocks is investigated (Figure 1). This is the

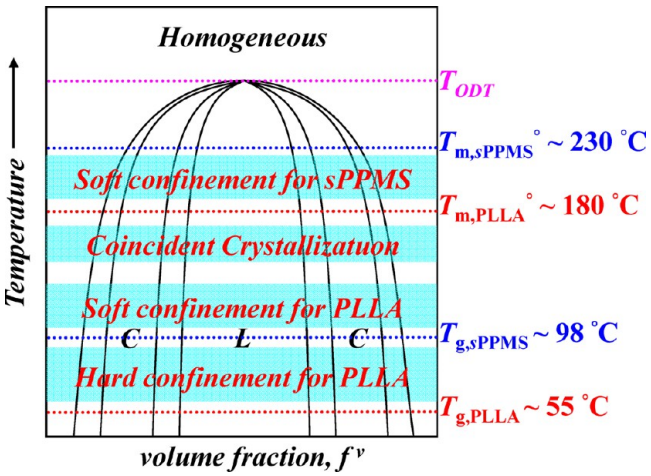

Figure 1. Interactive confinement in double-crystalline *s*PPMS−PLLA BCPs.

first system that various crystalline conditions including single, double, and coincident crystallizations under soft or hard confinement can be achieved in the same block copolymer by one- or two-stage crystallization process. Accordingly, the *s*PPMS−PLLA BCPs having diverse crystalline conditions can give a systematical study to exploit the effects of the crystallization sequence, microstructural shape, segregation strength, and vitrification on the final crystalline morphologies without the alternation of chemical compositions. As a result, with the control of interactive crystallization, ordered nanoporous crystalline templates with different shapes were also fabricated using the degradable double-crystalline *s*PPMS−PLLA BCPs, providing a novel crystalline nanotemplate for applications.

EXPERIMENTAL SECTION

Materials and Sample Preparation. The *s*PPMS−PLLA BCPs were synthesized by controlled ring-opening polymerization of L-lactide using a hydroxyl-capped *s*PPMS as the macroinitiator. The detailed synthetic method was reported previously.[51] The volume fraction of the PLLA block was calculated by assuming that the densities of *s*PPMS and PLLA are 1.02 and 1.25 g/cm^3, respectively. The characteristic features of the samples are listed in Table 1. Bulk samples of the *s*PPMS−PLLA BCPs were prepared by solution casting from a nonselective solvent, dichloromethane (CH_2Cl_2), at a polymer concentration of 10 wt %. After complete dissolution of the given BCP, the solution was then transferred in a vial sealed by aluminum foil having one punched hole for slow evaporation of CH_2Cl_2 at atmosphere for 3 days. This can give long-range-order nanostructures with less defects and grain boundaries. With further drying in a vacuum oven for 24 h to remove the residual solvent, the bulk samples could be thus obtained.

Table 1. Characteristics of *s*PPMS−PLLA BCPs

sample	$M_{n,sPPMS}$ (g/mol)	$M_{n,PLLA}$ (g/mol)	$M_{n,total}$ (g/mol)	PDI	f_{PLLA}^v
*s*PPMS11−PLLA5	11000	4900	15900	1.24	0.27
*s*PPMS11−PLLA10	11000	9800	20800	1.21	0.42

Fabrication of Nanoporous *s*PPMS−PLLA. The PLLA microdomains in the *s*PPMS−PLLA can be selectively degenerated through hydrolysis in a 0.5 M base solution (2 g of sodium hydroxide in a 40/60 (v/v) solution of deionized water and methanol) at 45 °C for 5 days. After rinsing by the water/methanol mixture, nanoporous templates were prepared.

Differential Scanning Calorimetry (DSC). The bulk samples were first heated to 230 °C (above the melting points of both *s*PPMS and PLLA) for 1 min to eliminate the thermal history from the solvent casting procedure using a PerkinElmer Pyris1 equipped with a compressor of Intracooler 2P. The samples were then slowly cooled to 25 °C at a rate of 10 °C/min for nonisothermal crystallization. For the experiment of isothermal crystallization, the samples melted at 230 °C were rapidly cooled to a preset crystallization temperature, T_c, at a rate of 150 °C/min. The melting temperature, T_m, and its endotherm were recorded during heating at a scan rate of 10 °C/min in DSC with the calibration by standard materials of cyclohexane and indium. Each sample weight was 5 mg for all treatments in DSC.

Transmission Electron Microscopy (TEM). Bulk samples of the *s*PPMS−PLLA BCPs were microtomed at room temperature for transmission electron microscopic (TEM) observation. Ultramicrosection is carried out using a Reicher Ulracut microtome equipped with a diamond knife. To enhance the mass−thickness contrast under TEM observation, staining was conducted by exposing the microsectioned slices to a vapor of a 4% aqueous RuO_4 solution for 1 h. Bright-field TEM images were obtained on a JEOL JEM-2100 TEM at an accelerating voltage of 200 kV. After RuO_4 staining, the *s*PPMS microdomains are dark and the PLLA microdomains are bright under TEM.

Field-Emission Scanning Electron Microscopy (FESEM). The nanoposous samples were sputter-coated with a thin gold layer to reduce charging effect under FESEM observation. Nanoporous structures of the hydrolyzed samples were probed using a FESEM of JEOL JSM-6700F at an accelerating voltage of 5 kV.

X-ray Experiments. Simultaneous small-angle X-ray scattering (SAXS) and wide-angle X-ray diffraction (WAXD) experiments were conducted using the synchrotron X-ray beamline 23A at the National Synchrotron Research Center (NSRRC) in Taiwan.[52] The wavelength λ of the X-ray beam was 0.0827 nm. A Pilatus-1MF pixel detector with an active area of 169 × 179 mm^2 having the pixel resolution of 172 mm was

DOI: 10.1021/acs.macromol.6b01725
Macromolecules XXXX, XXX, XXX−XXX

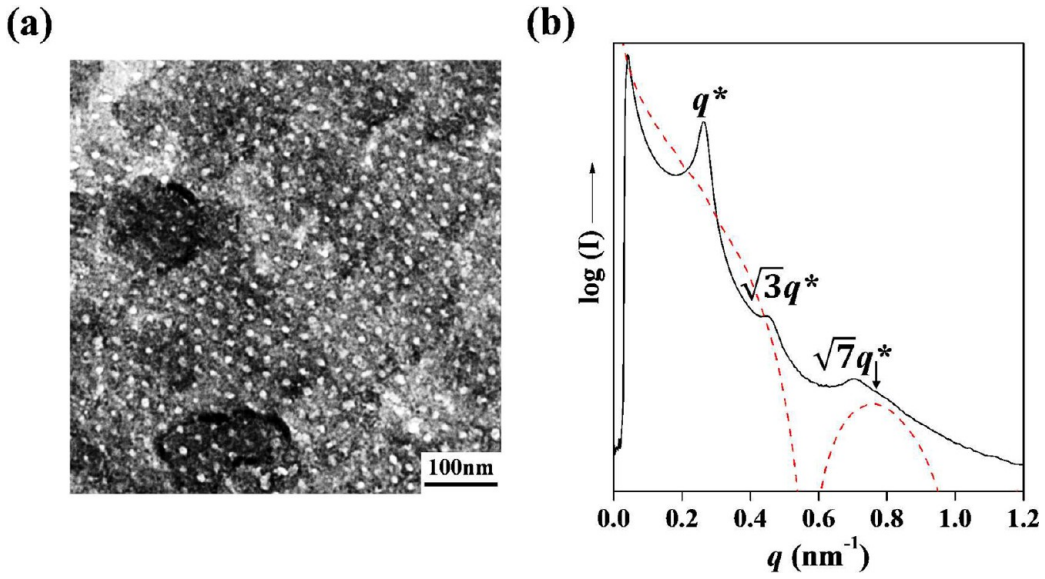

Figure 2. (a) TEM micrograph and (b) 1D SAXS profile of the *s*PPMS11−PLLA5 after quenched from the melt at 230 °C. The dashed line shows the form factor fitting curve of the cylinder having the diameter of 13.5 nm. With RuO_4 staining, the bright region is PLLA and dark area is *s*PPMS.

utilized for collecting the two-dimensional (2D) patterns. One-dimensional (1D) SAXS profiles were obtained by azimuthal integration from the 2D SAXS patterns. The scattering angle of the SAXS pattern was calibrated by the first-order scattering vector of silver behenate, i.e., $q^* = 1.076\ nm^{-1}$ ($q^* = 4\pi\lambda^{-1} \sin\theta$, where 2θ is the scattering angle enclosed by the incident and scattering beams). A 2D flat panel detector (C9728DK-10, Hamamatsu Japan) was utilized for collecting the 2D WAXD patterns. 1D WAXD profiles were obtained by azimuthal integration of the corresponding 2D WAXD patterns. The positions and widths of the observed diffraction peak were calibrated with silicon powder.

Normalized 1D Correlation Function. The normalized 1D correlation function $[\gamma(z)]$ can be calculated using the following equation:[53,54]

$$\gamma(z) = \frac{1}{Q}\int_0^\infty q^2 I(q)\cos(qz)\,dq$$

where q is the scattering vector, $I(q)$ is intensity of the observed 1D SAXS pattern, z is the coordinate along the electron density distribution, and the invariant Q is the integrated scattering intensity as a function of q, described by the equation

$$Q = \int_0^\infty q^2 I(q)\,dq$$

First, thermal fluctuations were subtracted from the observed scattering intensity by calculating the slope of the plot of $I(q)q^4$ versus q^4 at wide scattering vector q to match the 1D correlation function. Therefore, the 1D correlation function, $\gamma(z)$, varied with the real space coordinate (z) was plotted using the previous normalized 1D correlation function. The thickness of the thinner layer was estimated from the intercept (for the real space coordinate axis) by the tangent line near the position at $z = 0$.

RESULTS AND DISCUSSION

Microphase Separation of *s*PPMS−PLLA BCPs Prior to Crystallization. The thermal properties of the *s*PPMS−PLLA BCPs were examined by differential scanning calorimetry (DSC). In Figure S1a, the *s*PPMS11−PLLA5 exhibits two glass transition temperatures of the *s*PPMS ($T_{g,sPPMS}$) and the PLLA ($T_{g,PLLA}$) blocks at 97.8 and 55.6 °C, respectively. Similarly, the $T_{g,sPPMS}$ and $T_{g,PLLA}$ in the *s*PPMS11−PLLA10 are found at 95.9 and 54.6 °C, respectively (Figure S1b). These observed T_gs are almost identical to those of the neat *s*PPMS and PLLA homopolymers,[55,56] revealing strong incompatibility between the *s*PPMS and PLLA blocks. This can be also confirmed by the large difference in the solubility parameters between the *s*PPMS (δ_{sPPMS} = 9.4 $cal^{0.5}\ cm^{-1.5}$) and PLLA (δ_{PLLA} = 10.9 $cal^{0.5}\ cm^{-1.5}$).[57,58]

The microphase-separated morphologies before crystallization were explored using transmission electron microscopy (TEM) and small-angle X-ray scattering (SAXS). The samples for TEM and SAXS measurements were first heated to 230 °C at a rate of 10 °C for 1 min and then rapidly quenched into liquid nitrogen for 5 min. In Figure 2a, the TEM micrograph reveals that hexagonally packed PLLA cylinders in a *s*PPMS matrix can be obtained in the *s*PPMS11−PLLA5 after quenched from the melt at 230 °C. The corresponding one-dimensional (1D) SAXS profile displays intense reflections at the relative q^* ratios of $1:\sqrt{3}:\sqrt{7}$ (Figure 2b), indicating the formation of the hexagonally packed cylinders with the long period of 27.5 nm. As determined by form factor fitting (dashed line in Figure 2b), the average diameter of the PLLA cylinders is 13.5 nm. As calculated, the TEM micrograph shows the cylindrical diameter of 13.1 nm in average. This value is smaller than that calculated from form factor fitting (13.5 nm) due to the projection effect.

In contrast, the *s*PPMS11−PLLA10 displays lamellar nanostructures (Figure 3a), which is identical to the 1D SAXS profile exhibiting the lamellar reflections of 1:2:3:4 (Figure 3b). As calculated by the primary peak, the lamellar long period is 25.5 nm. Using normalized 1D correlation function $\gamma(z)$ allows us to determine the respective thicknesses of the *s*PPMS (d_{sPPMS}) and PLLA (d_{PLLA}) microdomains. As shown in Figure 3c, the thinner thickness is 10.7 nm belonging to the PLLA microdomain due to the smaller volume fraction (f_{PLLA}^{v} = 0.42) than that of the *s*PPMS. This is almost consistent with the value of 10.6 nm estimated by BCP composition. These data are summarized in Table 2. Figure S2 shows the in-situ SAXS profiles of the *s*PPMS11−PLLA5 and *s*PPMS11−PLLA10 measured at 230 °C. As shown, the SAXS profiles still reveal the characteristic reflections of cylinder and lamellar nanostructures for the *s*PPMS11−PLLA5 and *s*PPMS11−PLLA10, respectively. This expresses the result that the cylinder and lamellar nanostructures still remain at the melt of 230 °C. The corresponding

DOI: 10.1021/acs.macromol.6b01725
Macromolecules XXXX, XXX, XXX−XXX

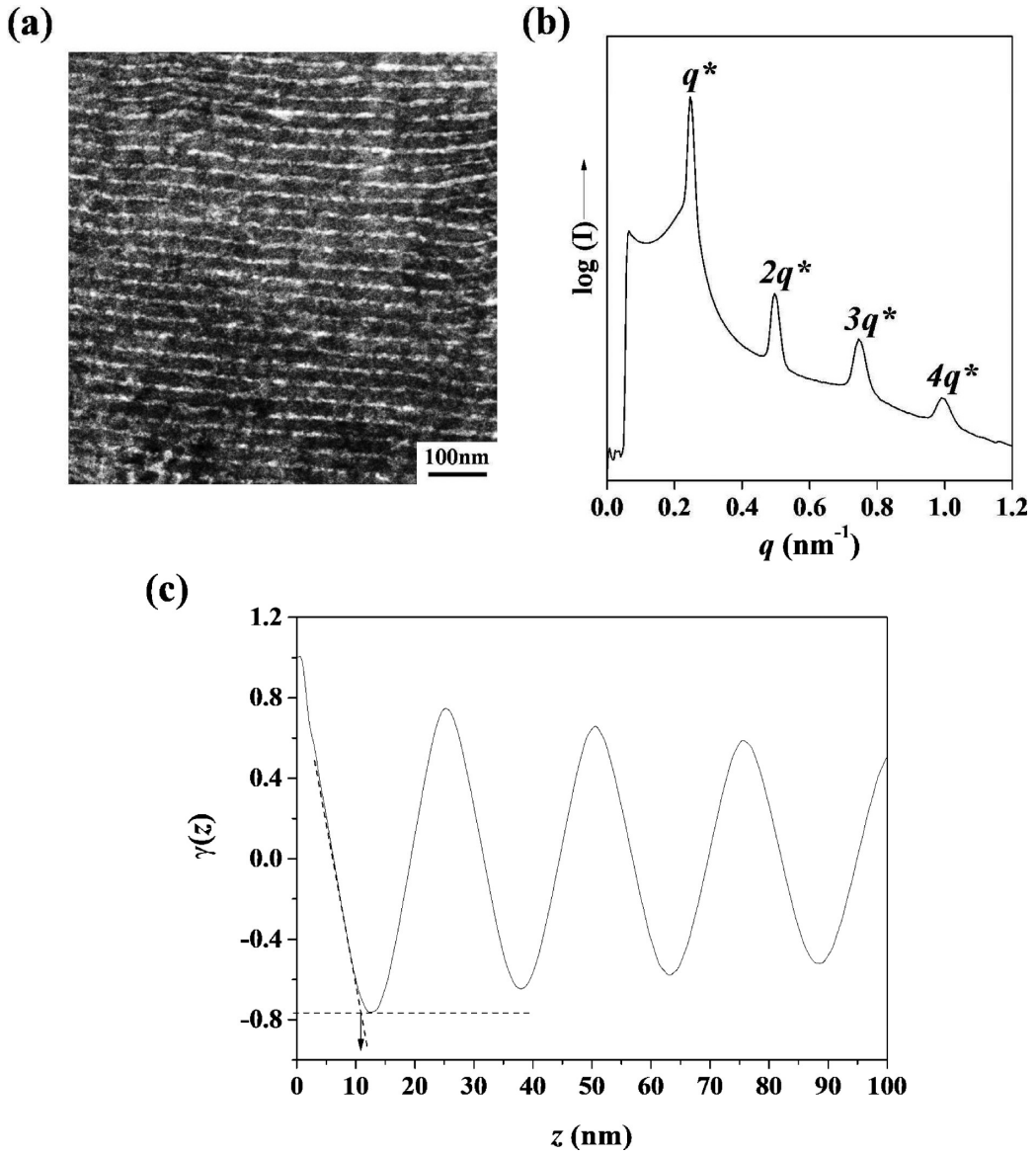

Figure 3. (a) TEM micrograph and (b) 1D SAXS profile of the *s*PPMS11−PLLA10 after quenched from the melt at 230 °C. (c) Profile of normalized 1D correlation function.

Table 2. Microstructural Parameters of *s*PPMS−PLLA BCPs

sample	morphology	long period[a] (nm)	PLLA thickness (d_{PLLA}) (nm)	*s*PPMS thickness of (d_{sPPMS}) (nm)
*s*PPMS11−PLLA10	lamella	25.5	10.7[b]	14.8
*s*PPMS11−PLLA5	cylinder	27.5	13.5[c]	14.0[d]

[a]Calculated by 1D SAXS profile. [b]Determined by normalized 1D correlation function. [c]Calculated from form factor fitting. [d]The minimum distance in-between two neighboring PLLA cylinders.

unstructured amorphous WAXD profiles of the quenched BCPs demonstrate that no crystallization occurs during the quenched process (Figure S3). This can be further confirmed by the absence of exothermic peaks of cold crystallization but T_g signals of *s*PPMS and PLLA found in the DSC heating scans for the quenched BCPs (Figure S1). Figure S4 shows the DSC profiles for nonisothermal crystallization of the lamella- and cylinder-structured *s*PPMS−PLLA BCPs, *s*PPMS, and PLLA homopolymers. As shown in the cooling scans at a rate of 10 °C/min, no exothermic peaks, i.e., crystallization, can be found in the lamella- and cylinder-structured *s*PPMS−PLLA BCPs from melt, whereas a significant exothermic peak can be observed at 96.5 °C in the PLLA homopolymer. The exothermic peak is also absent for the *s*PPMS homopolymer due to the intrinsic slow crystallization resulted from the bulky conformation of the *s*PPMS. As a result, the crystallization rates of the *s*PPMS and PLLA blocks are largely reduced in the nanoscale microphase separation.

Single Crystallization in *s*PPMS−PLLA BCPs. To detailed investigate the crystallization behavior of the *s*PPMS−PLLA BCPs, isothermal crystallization was first performed at a preset T_c, namely, one-stage crystallization. No endothermic peak could be found in the cylinder-structured *s*PPMS11−PLLA5 as T_cs = 90−120 °C. The absence of the PLLA crystallization is attributed to spatial confinement effect (i.e., shape effect).[59,60] In contrast, multiple melting peaks of the *s*PPMS ($T_{m,sPPMS}$) are found when the *s*PPMS11−PLLA5 crystallized at T_cs = 140−170 °C (Figure 4a), which is verified by the appearance of the characteristic reflections of the form II (2θ = 9.1°, 9.7°, 18°, and 21.4°) and

DOI: 10.1021/acs.macromol.6b01725
Macromolecules XXXX, XXX, XXX−XXX

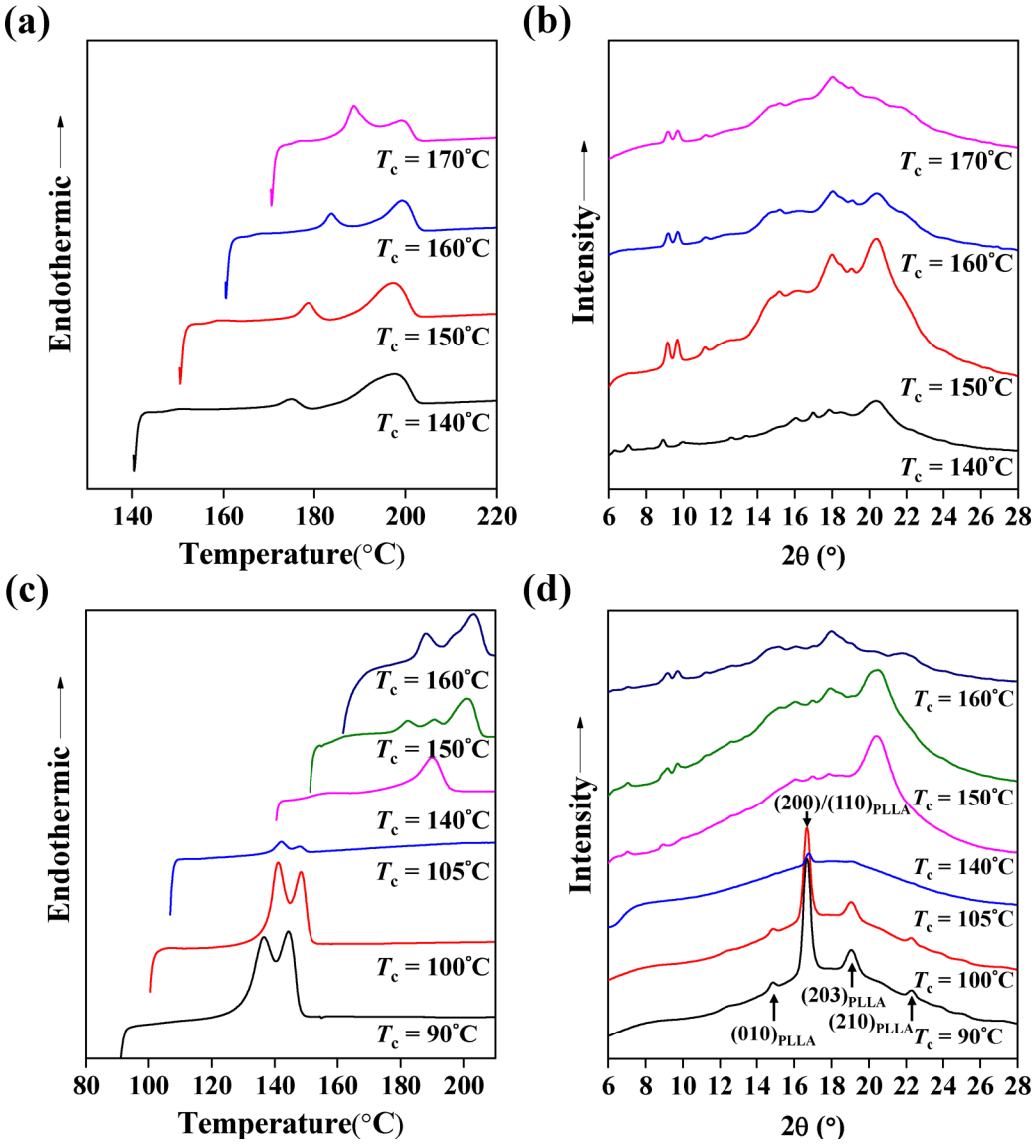

Figure 4. DSC thermograms and WAXD profiles of the *s*PPMS−PLLA crystallized isothermally at various temperatures: (a, b) for cylinder-structured *s*PPMS11−PLLA5; (c, d) for lamella-structured *s*PPMS11−PLLA10.

form III (2θ = 7.0° and 20.3°) crystals of the *s*PPMS (Figure 4b).[61−63]

Inversely, the melting peaks of the PLLA can be observed in the lamella-structured *s*PPMS11−PLLA10 at T_cs = 90−105 °C (Figure 4c), evidenced by the corresponding WAXD profile of the α-from PLLA crystal (Figure 4d).[64,65] As T_c = 105 °C, the reduced intensity of the $(200)_{PLLA}/(110)_{PLLA}$ reflections at 16.8° indicates a decrease in the crystallinity of the PLLA consistent with the DSC result in Figure 4c. As T_cs = 110−130 °C, the silent DSC and WAXD profiles indicate the noncrystalline *s*PPMS and PLLA. With elevating T_c up to 140−150 °C, multiple melting peaks of the *s*PPMS are found (Figure 4c). Unlike the single crystallizable *s*PPMS in the cylinder-structured *s*PPMS11−PLLA5, the crystallization event of the PLLA block at low temperature (90−105 °C) can be clearly separated from that of the *s*PPMS block at high temperature (140−160 °C) in the lamella-structured *s*PPMS11−PLLA10. This indicates that the interactive crystallization of the *s*PPMS and PLLA blocks can be manipulated in the lamella-structured *s*PPMS11−PLLA10.

After isothermal crystallization at various T_cs, the BCPs were rapidly quenched to 25 °C (far below $T_{g,PLLA}$ and $T_{g,sPPMS}$) to preserve the single-crystallized morphologies. The TEM micrograph reveals that the hexagonally packed PLLA cylinders are distorted by the *s*PPMS crystallization in the *s*PPMS11−PLLA5 crystallized at $T_{c,sPPMS}$ = 140 °C under soft confinement (i.e., $T_{c,sPPMS} > T_{g,PLLA}$) (Figure 5a). This can be confirmed by the corresponding 1D SAXS profile revealing only a scattering peak at low q region (Figure 5b). With increasing T_c to 150 °C, the hexagonally packed cylinders were completely broken to form breakout morphology (Figure 5c,d) due to weak segregation strength of the BCP microphase separation. Figure S5 shows the time-dependent SAXS profiles for the cylinder-structured *s*PPMS11−PLLA5 BCP isothermally crystallized at 150 °C. With the increase of the time period for isothermal crystallization, the SAXS profiles show that the high-order reflections progressively disappear and finally exhibit a broad peak after 2.5 h, indicating the formation of breakout morphology.

DOI: 10.1021/acs.macromol.6b01725
Macromolecules XXXX, XXX, XXX−XXX

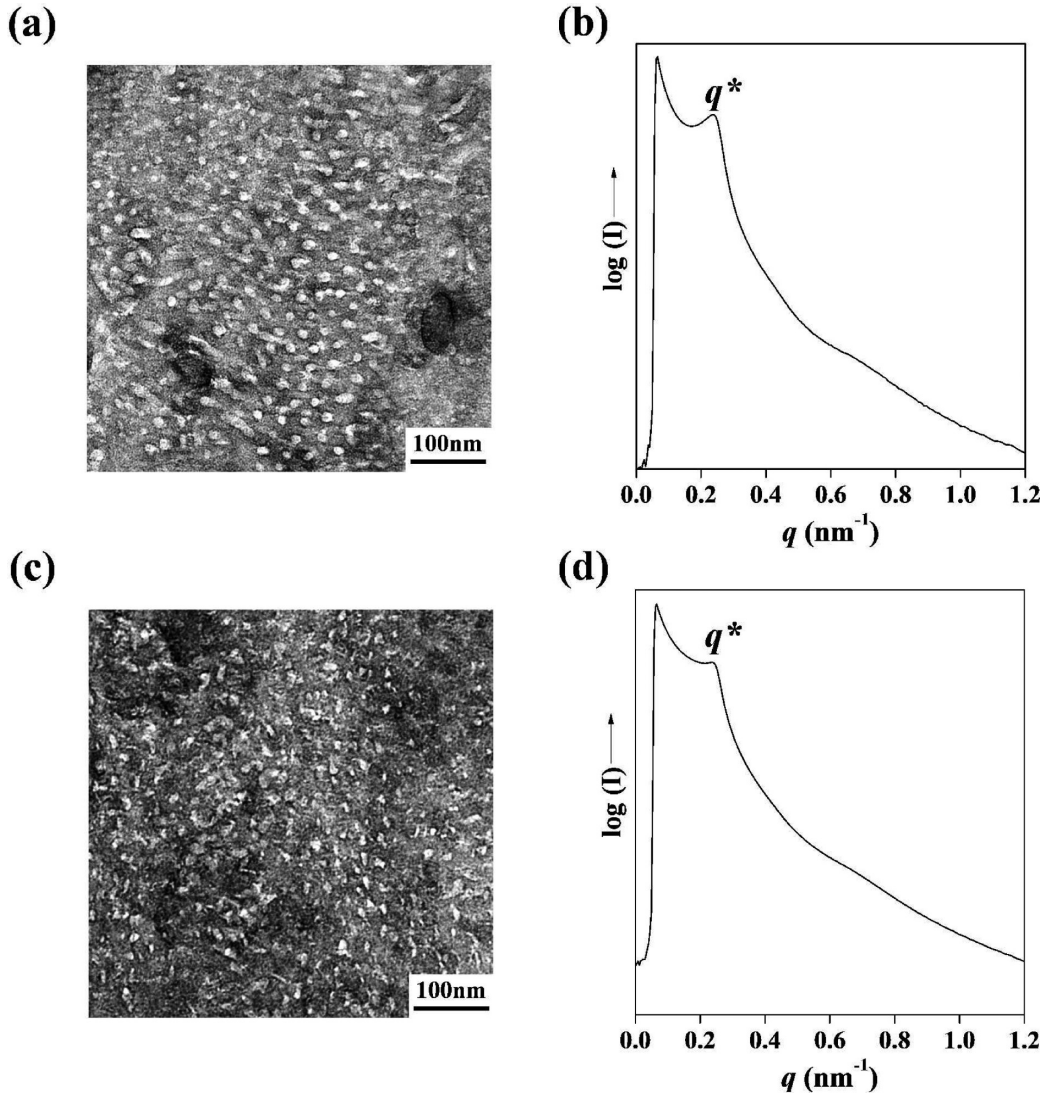

Figure 5. TEM micrographs and 1D SAXS profiles of the cylinder-structured *s*PPMS11−PLLA5 after crystallization at (a, b) 140 °C and (c, d) 150 °C for 3 h.

Regarding the single crystallization in the lamella-structured *s*PPMS11−PLLA10, the 1D SAXS profile at $T_{c,PLLA}$ = 90 °C exhibits sharp and intense reflections with the relative *q* ratios of 1:2:3:4 (Figure 6), indicating that the lamellar nanostructure remains unchanged under hard confinement (i.e., $T_{c,PLLA} < T_{g,sPPMS}$) due to the vitrified *s*PPMS microdomain. The well-defined lamellar nanostructure also confirms this result (Figure 7a). Notably, as $T_{c,PLLA}$ = 100 °C, similar confined lamellar nanostructure is obtained under soft confinement (i.e., $T_{c,PLLA} > T_{g,sPPMS}$), (Figures 6 and 7b). Consequently, the lamellar nanostructure can be preserved in the *s*PPMS11−PLLA10 despite the PLLA block crystallized under hard or soft confinement due to strong segregation strength of the BCP. Interestingly, when *s*PPMS crystallized at 140 °C, the coexistence of two different nanometer-sized lamellar nanostructures is observed in Figure 6. Except for the reflections at the *q* values of 0.234, 0.468, and 0.703 nm^{-1} resulted from the intrinsic microphase-separated lamellae, new lamellar reflections peaked at the lower *q* values of 0.189 and 0.377 nm^{-1} are simultaneously obtained (arrows in Figure 6), indicating the formation of dual-sized lamellae. This can be verified by the TEM micrograph in which two different nanometer-sized lamellar nanostructures are found in Figure 7c. As calculated, the long period of the new lamellar nanostructure is 33.2 nm, which is much larger than that of the intrinsic lamellae (26.9 nm). We suggest that the competitive result between the segregation strength of the BCP and the crystallization force of the *s*PPMS reaches a moderate state (or weakly confined state) that the crystal growth of the *s*PPMS nanocrystallite is templated along the lamellar nanostructure without breakout, giving the large-sized lamellae, namely, *s*PPMS-crystallization-induced thickening of microdomain. With the increase of T_c to 150 °C, a complete transformation to the large-sized lamellar nanostructure is obtained (Figures 6 and 7d). However, as T_c = 160 °C, the *s*PPMS nanocrystallite can isotropically grow and propagate to randomly penetrate the microdomains, giving the serious distortion of the intrinsic ordered lamellar nanostructure (Figure 7e), that is, breakout morphology. Also, this can be confirmed by only a broad scattering peak in the SAXS profile (Figure 6). As a result, the coexistence of dual-sized lamellar nanostructures is due to the growth of the inclusive *s*PPMS nanocrystallites templating along the ordered lamellar nanostructures under confinement. The final morphology of the single-crystallized *s*PPMS11−PLLA10 is strongly affected by the crystallization

DOI: 10.1021/acs.macromol.6b01725
Macromolecules XXXX, XXX, XXX−XXX

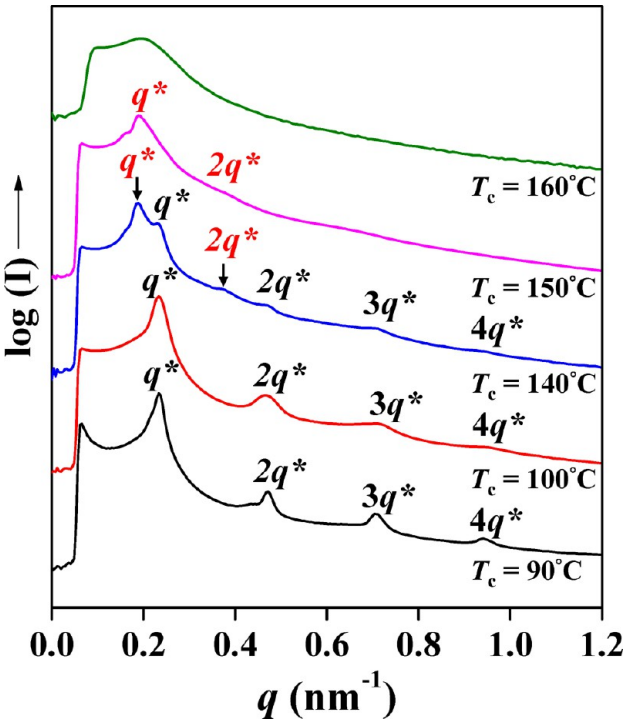

Figure 6. 1D SAXS profiles of the *s*PPMS11−PLLA10 after isothermal crystallization at various temperatures for 3 h.

temperature, exhibiting the morphological transition from the confined monosized lamella (T_c = 90−100 °C) to the metastable dual-sized lamella (T_c = 140 °C) and finally to the breakout morphology (T_c = 160 °C).

To further investigate the forming mechanism of the dual-sized lamellae, we conducted isothermal crystallization at T_c = 140 °C for different time periods (Figure 8a). After crystallization at 140 °C for 1 h, the appearance of the reflections at the lower q region indicates the formation of the large-sized lamella. Notably, with the continuous increase of the time period (1−6 h), the intensity of the lower q reflection increases, whereas the intrinsic reflection at higher q region decreases. Figure 8b shows the time-varied intensity of the primary scattering peaks for the intrinsic and large-sized lamellae. As shown, the opposite tendency for the two different nanometer-sized lamellae is observed. This expresses the result that the increased *s*PPMS crystallinity with time leads to the increased numbers of the large-sized lamella. As the time period ≥12 h, the 1D SAXS profile only reveals the reflections from the large-sized lamella (Figure 8a), indicating that the complete transform from the intrinsic to the large-sized lamella (Figure S6). The formation of the dual-sized lamellae is attributed to the kinetics of the crystalline growth of the *s*PPMS. As a result, the phase transition from small- to large-sized lamellar nanostructures can be triggered by elevating crystallization temperature thermodynamically and by increasing crystallinity kinetically.

Two-Stage and Coincident Double Crystallizations. The double-crystallized morphologies of the *s*PPMS11−PLLA10 BCP were investigated by two-stage crystallization with different sequences. We first crystallized *s*PPMS at higher temperature (140−160 °C) and then rapidly cooled the sample to lower temperature (100 °C) for PLLA crystallization (denoted as *s*PPMS → PLLA) (Figure 9a). Based on the WAXD profiles in Figure S7a, the double crystallization of the PLLA and *s*PPMS is obtained after the two-stage crystallization. In Figure 9a, the double-crystallized *s*PPMS11−PLLA10 with 140 → 100 °C, 150 → 100 °C, and 160 → 100 °C treatments also reveals dual-sized lamellae, the monosized lamella, and breakout morphology, respectively. The first-crystallized *s*PPMS could give a robust crystalline template for the confinement of the subsequent PLLA crystallization, namely, crystallization-driven confinement. As a result, the double-crystallized morphologies of the *s*PPMS11−PLLA10 are mainly determined by the first-crystallized event of the *s*PPMS.

To test the crystallization-driven confinement, we conducted the different sequences of two-stage crystallization, i.e., PLLA →

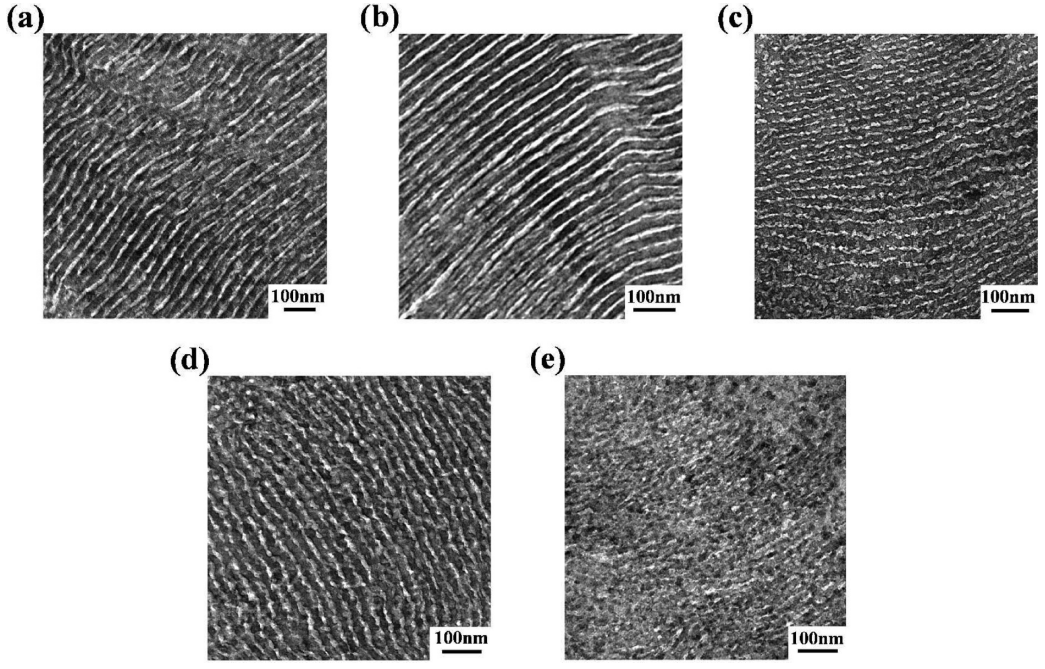

Figure 7. TEM micrographs of the *s*PPMS11−PLLA10 after isothermal crystallization at (a) 90, (b) 100, (c) 140, (d) 150, and (e) 160 °C for 3 h.

DOI: 10.1021/acs.macromol.6b01725
Macromolecules XXXX, XXX, XXX−XXX

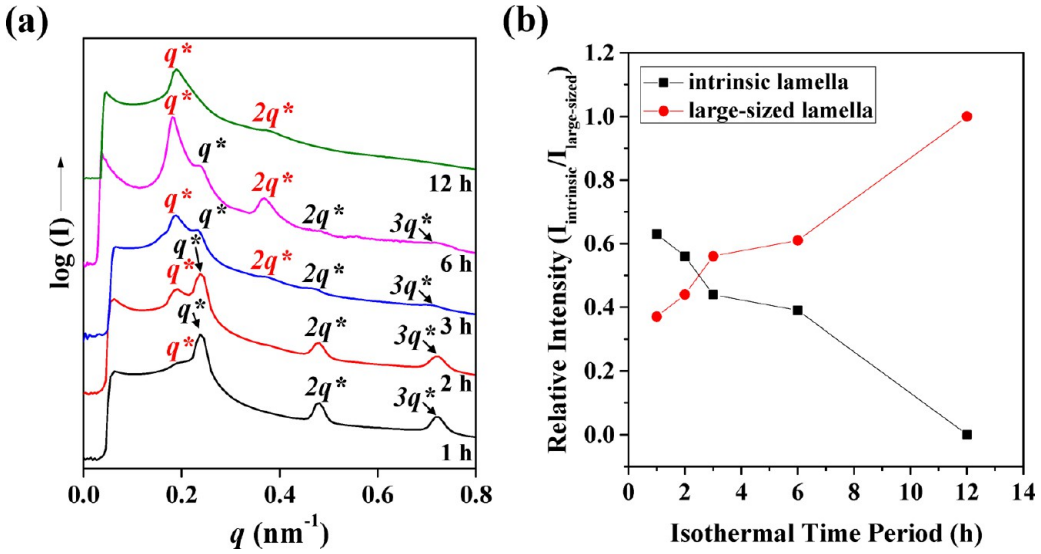

Figure 8. (a) 1D SAXS profiles of the *s*PPMS11−PLLA10 isothermally crystallized at 140 °C for various time periods. (b) Relative intensity of the primary peaks of the dual-sized lamellae varied with the time periods at T_c = 140 °C.

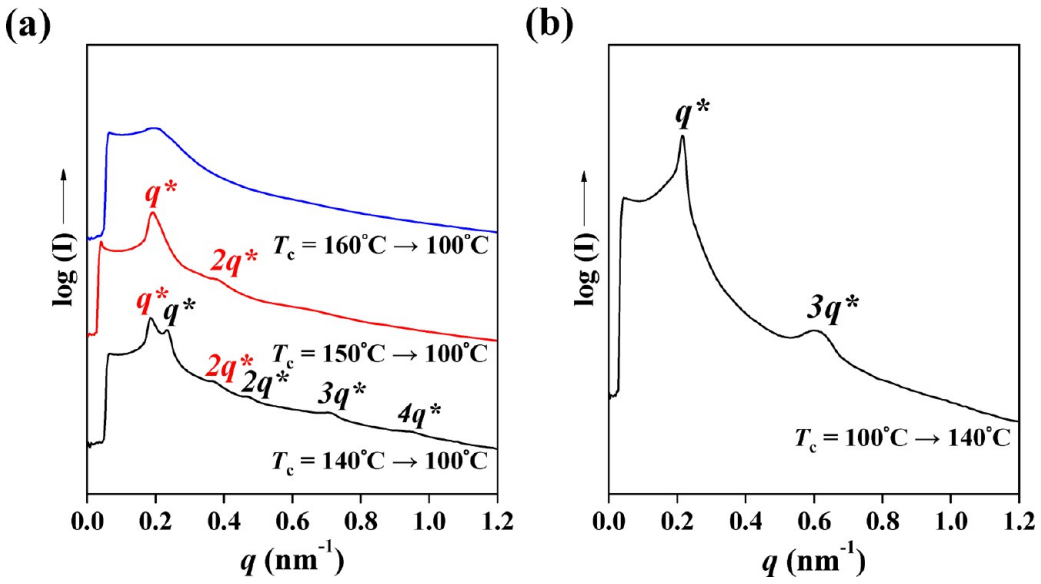

Figure 9. 1D SAXS profiles of (a) the *s*PPMS11−PLLA10 after two-stage crystallizations of 140 °C (3 h) → 100 °C (4 h), 150 °C (3 h) → 100 °C (4 h), 160 °C (3 h) → 100 °C (4 h), and (b) the *s*PPMS11−PLLA10 after two-stage crystallization of 100 °C (6 h) → 140 °C (3 h).

*s*PPMS (Figure 9b). The sample first crystallized at T_c = 100 °C for 6 h and then rapidly heated to 140 °C for 3 h, giving the double crystallization of the PLLA and *s*PPMS (Figure S7b). Interestingly, instead of the formation of dual-sized lamellae, the monosized lamellar nanostructure can be observed (Figure 9b), consistent with that after single crystallization of PLLA at T_c = 100 °C (Figure 6). Again, this confirms that the concept of the crystallization-driven confinement even though the subsequent T_c is far above the T_g of the first-crystallized block. As a result, interactive confinement by double crystallization with different sequences can be carried out in the lamella-structured *s*PPMS11−PLLA10.

Owing to the partial overlapping of the crystallization windows of PLLA and *s*PPMS, there should be a temperature range for coincident crystallization theoretically. Because of insufficient degree of supercooling and chain mobility for PLLA and *s*PPMS blocks, respectively, under confinement, the coincident crystallization, however, cannot be directly performed. Therefore, we conducted the self-seeding method to achieve the coincident crystallization in the study (Figure 10). First, the *s*PPMS11−PLLA10 was cooled from 230 °C to $T_{c,sPPMS}$ = 140 °C for 3 h and then was reheated to 188 °C (slightly below $T_{m,sPPMS}$) for 3 min to partially eliminate the *s*PPMS crystallites for the self-nucleation of the *s*PPMS. The sample was subsequently cooled to $T_{c,PLLA}$ = 100 °C for 4 h and then reheated to 142 °C (slightly below $T_{m,PLLA}$) for 3 min for the self-nucleation of the PLLA. Finally, the self-seeding sample was quenched to 120 °C (T_s = 120 °C) for 5 h to drive the coincident crystallization of both the PLLA and *s*PPMS. In accordance with the WAXD profile (Figure 10b), the coexistence of the PLLA and *s*PPMS crystals is obtained, confirming the coincident crystallization. The relative *q* ratios of 1:2:3 in the 1D SAXS profile indicates the preserved lamellar nanostructure (Figure 10a). Notably, the long period (30 nm) calculated form the primary peak is slightly larger than

DOI: 10.1021/acs.macromol.6b01725
Macromolecules XXXX, XXX, XXX−XXX

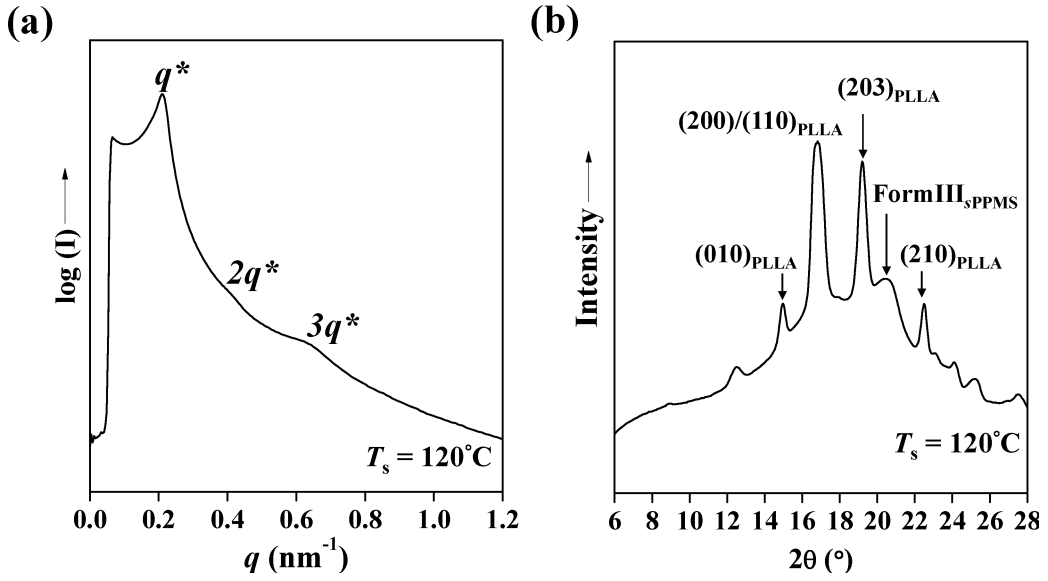

Figure 10. (a) 1D SAXS and (b) the corresponding WAXD profiles of the self-seeding *s*PPMS11−PLLA10 after crystallization at 120 °C for 5 h.

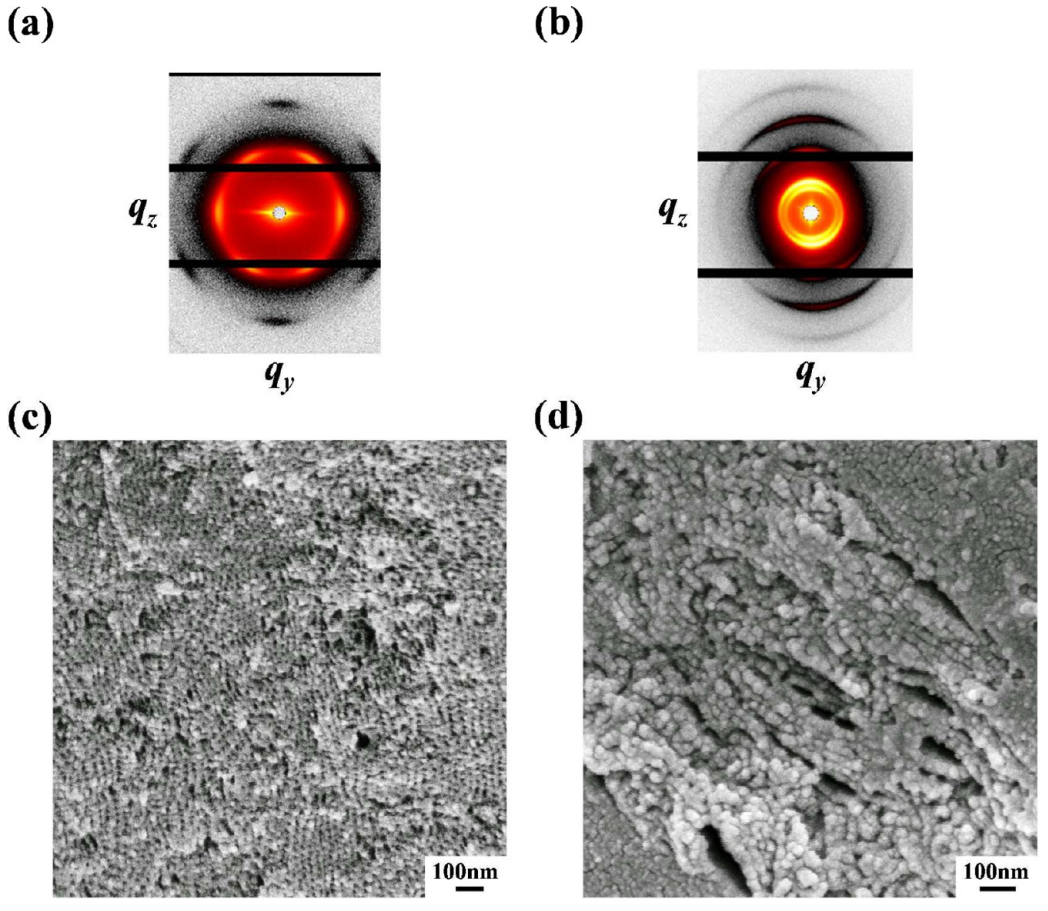

Figure 11. 2D SAXS patterns of the shear-aligned (a) *s*PPMS11−PLLA5 and (b) *s*PPMS11−PLLA10 after crystallization at 140 °C for 3 h. FESEM micrographs of the crystallized (c) *s*PPMS11−PLLA5 and (d) *s*PPMS11−PLLA10 after hydrolysis of the PLLA.

that (28.2 nm) after two-stage double crystallization at 100 °C → 140 °C, suggesting weaker confinement in the coincidently crystallized process.

Nanoporous Crystalline Templates from Double-Crystalline BCPs. Degradable PLLA material is a well-known aliphatic polyester with easily decomposed feature by hydrolysis and is a good candidate for the preparation of nanoporous microstructures. To acquire well-oriented nanostructures, oscillatory shear force was applied onto the lamella- and cylinder-structured *s*PPMS−PLLA BCPs at 180 °C for 3 min. The as-sheared samples were subsequently quenched to 25 °C to preserve the shear-aligned morphologies. The shear-aligned

DOI: 10.1021/acs.macromol.6b01725
Macromolecules XXXX, XXX, XXX−XXX

samples then crystallized at 140 °C so as to fabricate crystalline *s*PPMS templates. In Figures 11a and 11b, the 2D SAXS patterns show well-defined anisotropic reflections of the hexagonally packed and layered arcs, respectively, indicating the formation of the highly aligned large-area cylindrical and lamellar nanostructures. After hydrolysis, the cross-sectional FESEM micrograph reveals that the well-ordered crystalline nanochannels packed in a hexagonal lattice are obtained in the *s*PPMS11−PLLA5 BCP (Figure 11c). In contrast to the distorted morphology in Figure 5a, we suggest that the oriented sample may have more stable morphology against crystallization due to the reduced numbers of defects. Also, the crystalline nanosheets can be observed in the hydrolyzed *s*PPMS11−PLLA10 BCP (Figure 11d). The thermal resistance of the crystalline nanoporous template is also tested. After isothermal annealing at 90 °C for 10 min, the crystalline nanochannels can still be observed (Figure S8a), whereas the collapse of the nanochannels is obtained in the noncrystalline template (Figure S8b). This indicates that the *s*PPMS crystallization can elevate the thermal resistance of the nanoporous template. Consequently, this provides a novel robust crystalline nanoporous template featuring a percolating pore structure with a narrow pore size distribution.

CONCLUSION

The crystalline morphologies of the *s*PPMS−PLLA BCP are strongly dominated by the competition between the segregation strength of microphase separation and the crystalline force of the blocks. Instead of keeping the cylindrical nanostructure, the breakout morphology is obtained in the cylinder-structured *s*PPMS11−PLLA5 as the crystallization temperature is increased. Despite the PLLA block crystallized under hard or soft confinement, the lamellar nanostructure is preserved in the lamella-structured *s*PPMS11−PLLA10 BCP. Interestingly, a specific phase transition from the dual-sized to the monosized lamellae and finally to the breakout morphology is observed with increased crystallization temperature or crystalline time period of the *s*PPMS. Also, the crystallization-driven confinement by the first-crystallized event mainly determines the double-crystallized morphologies. With the control of interactive confinement, crystalline nanosheets and nanoporous cylindrical monoliths can be successfully fabricated.

ASSOCIATED CONTENT

Supporting Information

The Supporting Information is available free of charge on the ACS Publications website at DOI: 10.1021/acs.macromol.6b01725.

DSC heating curves of the *s*PPMS11−PLLA5 and *s*PPMS11−PLLA10 after quenched from the melt; 1D SAXS profiles of the *s*PPMS−PLLA BCPs measured at 230 °C; WAXD profiles of the *s*PPMS−PLLA BCPs after quenching from the melt at 230 °C; DSC cooling curves of the lamella-structured *s*PPMS11−PLLA10, cylinder-structured *s*PPMS11−PLLA10, *s*PPMS11−PLLA5, *s*PPMS homopolymer and PLLA homopolymer from the melt; 1D SAXS profiles of the *s*PPMS11−PLLA5 isothermally crystallized at 150 °C for various time periods; TEM micrograph of the *s*PPMS11−PLLA10 after isothermal crystallization at 140 °C for 12 h; WAXD profiles of the *s*PPMS11−PLLA10 after two-stage crystallization of 140 °C (3 h) → 100 °C (4 h), 150 °C (3 h) → 100 °C (4 h), and 160 °C (3 h) → 100 °C (4 h), and the *s*PPMS11−PLLA10 after two-stage crystallization of 100 °C (6 h) → 140 °C (3 h); FESEM micrographs of the crystallized (140 °C for 3 h) and noncrystalline *s*PPMS11−PLLA5 after the hydrolysis of the PLLA and followed by thermal annealing at 90 °C for 10 min (PDF)

AUTHOR INFORMATION

Corresponding Author

*Tel +886-7-5252000; Fax +886-5-5254099; e-mail ywchiang@mail.nsysu.edu.tw (Y.-W.C.).

Notes

The authors declare no competing financial interest.

ACKNOWLEDGMENTS

Authors thank Mr. Hsien-Tsan Lin of Regional Instruments Center at National Sun Yat-Sen University for his help in TEM experiments. We also thank and Drs. U-Ser Jeng and Chun-Jen Su of National Synchrotron Radiation Research Center (Taiwan) for their help in synchrotron SAXS experiments. Finally, authors appreciate the Ministry of Science and Technology of the Republic of China, Taiwan, for financially supporting this research (MOST 104-2221-E-110-073).

REFERENCES

(1) Bates, F. S.; Fredrickson, G. H. Block Copolymer Thermodynamics: Theory and Experiment. *Annu. Rev. Phys. Chem.* **1990**, *41*, 525−557.

(2) Bates, F. S.; Fredrickson, G. H. Block copolymers—Designer Soft Materials. *Phys. Today* **1999**, *52*, 32−38.

(3) Park, C.; Yoon, J.; Thomas, E. L. Enabling Nanotechnology with Self Assembled Block Copolymer Patterns. *Polymer* **2003**, *44*, 6725−6760.

(4) Uehara, H.; Kakiage, M.; Sekiya, M.; Yamagishi, T.; Yamanobe, T.; Nakajima, K.; Watanabe, T.; Nomura, K.; Hase, K.; Matsuda, M. Novel Design Solving the Conductivity vs Water-uptake Trade-off for Polymer Electrolyte Membrane by Bicontinuous Crystalline/Amorphous Morphology of Block Copolymer. *Macromolecules* **2009**, *42*, 7627−7630.

(5) Chiang, Y. W.; Huang, Y. W.; Huang, S. H.; Huang, P. S.; Mao, Y. C.; Tsai, C. K.; Kang, C. S.; Tasi, J.-C.; Su, C. J.; Jeng, U. S.; Tseng, W. H. Control of Nanostructural Dimension by Crystallization in a Double-Crystalline Syndiotactic Poly(4-methyl-1-pentene)-*block*-poly(L-lactide) Block Copolymer. *J. Phys. Chem. C* **2014**, *118*, 19402−19414.

(6) Chiang, Y. W.; Hu, Y. Y.; Li, J. N.; Huang, S. H.; Kuo, S. W. Trilayered Single Crystals with Epitaxial Growth in Poly(ethylene oxide)-*block*-poly(ε-caprolactone)-*block*-poly(L-lactide) Thin Films. *Macromolecules* **2015**, *48*, 8526−8533.

(7) Castillo, R. V.; Müller, A. J. Crystallization and Morphology of Biodegradable or Biostable Single and Double Crystalline Block Copolymers. *Prog. Polym. Sci.* **2009**, *34*, 516−560.

(8) He, W. N.; Xu, J. T. Crystallization Assisted Self-assembly of Semicrystalline Block Copolymers. *Prog. Polym. Sci.* **2012**, *37*, 1350−1400.

(9) Takeshita, H.; Shiomi, T.; Takenaka, K.; Arai, F. Crystallization and Higher-order Structure of Multicomponent Polymeric Systems. *Polymer* **2013**, *54*, 4776−4789.

(10) Huang, S.; Jiang, S. Structures and Morphologies of Biocompatible and Biodegradable Block Copolymers. *RSC Adv.* **2014**, *4*, 24566−24583.

(11) Nakagawa, S.; Marubayashi, H.; Nojima, S. Crystallization of Polymer Chains Confined in Nanodomains. *Eur. Polym. J.* **2015**, *70*, 262−275.

(12) Michell, R. M.; Müller, A. J. Confined Crystallization of Polymeric Materials. *Prog. Polym. Sci.* **2016**, *54*−*55*, 183−213.

DOI: 10.1021/acs.macromol.6b01725
Macromolecules XXXX, XXX, XXX−XXX

(13) Zha, L.; Hu, W. Molecular Simulations of Confined Crystallization in the Microdomains of Diblock Copolymers. *Prog. Polym. Sci.* **2016**, *54*−*55*, 232−258.
(14) Müller, A. J.; Balsamo, V.; Arnal, M. L. In *Lecture Notes in Physics: Progress in Understanding of Polymer Crystallization*; Reiter, G., Strobl, G., Eds.; Springer: Berlin, 2007; Vol. *714*, pp 229−259.
(15) Kim, K. S.; Chung, S.; Chin, I. J.; Kim, M. N.; Yoon, J. S. Crystallization Behavior of Biodegradable Amphiphilic Poly(ethylene glycol)-poly(L-lactide) Block Copolymers. *J. Appl. Polym. Sci.* **1999**, *72*, 341−348.
(16) Maglio, G.; Migliozzi, A.; Palumbo, R. Thermal Properties of Di- and Triblock Copolymers of Ppoly(L-lactide) with Poly(oxyethylene) or Poly(ε-caprolactone). *Polymer* **2003**, *44*, 369−375.
(17) Sun, L.; Liu, Y.; Zhu, L.; Hsiao, B. S.; Avila-Orta, C. A. Self-assembly and Crystallization Behavior of a Double-crystalline Polyethylene-*block*-poly(ethylene oxide) Diblock Copolymer. *Polymer* **2004**, *45*, 8181−8193.
(18) Nojima, S.; Akutsu, Y.; Washino, A.; Tanimoto, S. Morphology of Melt-Quenched Poly(ε-caprolactone)-*block*-polyethylene Copolymers. *Polymer* **2004**, *45*, 7317−7324.
(19) Nojima, S.; Akutsu, Y.; Akaba, M.; Tanimoto, S. Crystallization Behavior of Poly(ε-caprolactone) Blocks Starting from Polyethylene Lamellar Morphology in Poly(ε-caprolactone)-*block*-polyethylene Copolymers. *Polymer* **2005**, *46*, 4060−4067.
(20) Hamley, I. W.; Castelletto, V.; Castillo, R. V.; Müller, A. J.; Martin, C. M.; Pollet, E.; Dubois, P. Crystallization in Poly(L-lactide)-*b*-poly(ε-caprolactone) Double Crystalline Diblock Copolymers: A Study Using X-ray Scattering, Differential Scanning Calorimetry, and Polarized Optical Microscopy. *Macromolecules* **2005**, *38*, 463−47.
(21) Nojima, S.; Kiji, T.; Ohguma, Y. Characteristic Melting Behavior of Double Crystalline Poly(ε-caprolactone)-*block*-polyethylene Copolymers. *Macromolecules* **2007**, *40*, 7566−7572.
(22) Castillo, R. V.; Arnal, M. L.; Müller, A. J.; Hamley, I. W.; Castelletto, V.; Schmalz, H.; Abetz, V. Fractionated Crystallization and Fractionated Melting of Confined PEO Microdomains in PB-*b*-PEO and PE-*b*-PEO Diblock Copolymers. *Macromolecules* **2008**, *41*, 879−889.
(23) Weiyu, C.; Tashiro, K.; Hanesaka, M.; Takeda, S.; Masunaga, H.; Sasaki, S.; Takata, M. Relationship between Morphological Change and Crystalline Phase Transitions of Polyethylene-Poly(ethylene Oxide) Diblock Copolymers, Revealed by the Temperature-dependent Synchrotron WAXD/SAXS and Infrared/Raman Spectral Measurements. *J. Phys. Chem. B* **2009**, *113*, 2338−2346.
(24) Castillo, R. V.; Müller, A. J.; Raquez, J. M.; Dubois, P. Crystallization Kinetics and Morphology of Biodegradable Double Crystalline PLLA-*b*-PCL Diblock Copolymers. *Macromolecules* **2010**, *43*, 4149−4160.
(25) Cong, Y. H.; Liu, H.; Wang, D. L.; Zhao, B. J.; Yan, T. Z.; Li, L. B.; Chen, W.; Zhong, Z. Y.; Lin, M. C.; Chen, H. L.; Yang, C. L. Stretch-Induced Crystallization through Single Molecular Force Generating Mechanism. *Macromolecules* **2011**, *44*, 5878−5882.
(26) Li, S.; Myers, S. B.; Register, R. A. Solid-State Structure and Crystallization in Double-Crystalline Diblock Copolymers of Linear Polyethylene and Hydrogenated Polynorbornene. *Macromolecules* **2011**, *44*, 8835−8844.
(27) Yang, J. J.; Liang, Y. R.; Luo, J.; Zhao, C. Z.; Han, C. C. Multilength Scale Studies of the Confined Crystallization in Poly(L-lactide)-*block*-Poly(ethylene glycol) Copolymer. *Macromolecules* **2012**, *45*, 4254−4261.
(28) Lin, M. C.; Chen, H. L.; Su, W. B.; Su, C. J.; Jeng, U. S.; Tzeng, F. Y.; Wu, J. Y.; Tsai, J. C.; Hashimoto, T. Interactive Crystallization Kinetics in Double-Crystalline Block Copolymer. *Macromolecules* **2012**, *45*, 5114−5127.
(29) Shi, W.; McGrath, A. J.; Li, Y.; Lynd, N. A.; Hawker, C. J.; Fredrickson, G. H.; Kramer, E. J. Cooperative and Sequential Phase Transitions in *it*-Poly(propylene oxide)-*b*-poly(ethylene oxide)-*b*-*it*-poly(propylene oxide) Triblock Copolymers. *Macromolecules* **2015**, *48*, 3069−3079.
(30) Nojima, S.; Ono, M.; Ashida, T. Crystallization of Block Copolymers II. Morphological Study of Poly(ethylene glycol)-poly(ε-caprolactone) Block Copolymers. *Polym. J.* **1992**, *24*, 1271−1280.
(31) Gan, Z. H.; Jiang, B. Z.; Zhang, J. Poly(ε-caprolactone)/Poly(ethylene oxide) Diblock Copolymer. I. Isothermal Crystallization and Melting Behavior. *J. Appl. Polym. Sci.* **1996**, *59*, 961−967.
(32) Bogdanov, B.; Vidts, A.; Schacht, E.; Berghmans, H. Isothermal Crystallization of Poly(ε-caprolactone-ethylene glycol) Block Copolymers. *Macromolecules* **1999**, *32*, 726−731.
(33) Shiomi, T.; Imai, K.; Takenaka, K.; Takeshita, H.; Hayashi, H.; Tezuka, Y. Appearance of Double Spherulites Like Concentric Circles for Poly(ε-caprolactone)-*block*-poly(ethylene glycol)-*block*-poly(ε-caprolactone). *Polymer* **2001**, *42*, 3233−3239.
(34) Albuerne, J.; Marquez, L.; Müller, A. J.; Raquez, J. M.; Degee, P.; Dubois, P.; Castelletto, V.; Hamley, I. W. Nucleation and Crystallization in Double Crystalline Poly(*p*-dioxanone)-*b*-poly(ε-caprolactone) Diblock Copolymers. *Macromolecules* **2003**, *36*, 1633−1644.
(35) Ruokolainen, J.; Mezzenga, R.; Fredrickson, G. H.; Kramer, E. J.; Hustad, P. D.; Coates, G. W. Morphology and Thermodynamic Behavior of Syndiotactic Polypropylene-poly(ethylene-co-propylene) Block Polymers Prepared by Living Olefin Polymerization. *Macromolecules* **2005**, *38*, 851−860.
(36) Takeshita, H.; Fukumoto, K.; Ohnishi, T.; Ohkubo, T.; Miya, M.; Takenaka, K.; Shiomi, T. Formation of Lamellar Structure by Competition in Crystallization of Both Components for Crystalline-crystalline Block Copolymers. *Polymer* **2006**, *47*, 8210−8218.
(37) Castillo, R. V.; Müller, A. J.; Lin, M. C.; Chen, H. L.; Jeng, U. S.; Hillmyer, M. A. Confined Crystallization and Morphology of Melt Segregated PLLA-*b*-PE and PLDA-*b*-PE Diblock Copolymers. *Macromolecules* **2008**, *41*, 6154−6164.
(38) Myers, S. B.; Register, R. A. Crystalline-crystalline Diblock Copolymers of Linear Polyethylene and Hydrogenated Polynorbornene. *Macromolecules* **2008**, *41*, 6773−6779.
(39) Tzeng, F. Y.; Lin, M. C.; Wu, J. Y.; Kuo, J. C.; Tsai, J. C.; Hsiao, M. S.; Chen, H. L.; Cheng, S. Z. D. Stereoregular Diblock Copolymers of Syndiotactic Polypropylene and Polyesters: Syntheses and Self-assembled Nanostructures. *Macromolecules* **2009**, *42*, 3073−3085.
(40) Nojima, S.; Fukagawa, Y.; Ikeda, H. Interactive Crystallization of a Strongly Segregated Double Crystalline Block Copolymer with Close Crystallizable Temperatures. *Macromolecules* **2009**, *42*, 9515−9522.
(41) Voet, V. S.; van Ekenstein, G. O. A.; Meereboer, N. L.; Hofman, A. H.; ten Brinke, G.; Loos, K. Double-crystalline PLLA-*b*-PVDF-*b*-PLLA Triblock Copolymers: Preparation and Crystallization. *Polym. Chem.* **2014**, *5*, 2219−2230.
(42) Nagarajan, S.; Gowd, E. B. Cold Crystallization of PDMS and PLLA in Poly(L-lactide-*b*-dimethylsiloxane-*b*-L-lactide) Triblock Copolymer and Their Effect on Nanostructure Morphology. *Macromolecules* **2015**, *48*, 5367−5377.
(43) Thurn-Albrecht, T.; Steiner, R.; DeRouchey, J.; Stafford, C. M.; Huang, E.; Bal, M.; Tuominen, M.; Hawker, C. J.; Russell, T. P. Nanoscopic templates from oriented block copolymer films. *Adv. Mater.* **2000**, *12*, 787−791.
(44) Park, M.; Harrison, C.; Chaikin, P. M. Register, R. A.; Adamson, D. H. Block copolymer lithography: periodic arrays of$\sim 10^{11}$ holes in 1 square centimeter. *Science* **1997**, *276*, 1401−1404.
(45) Zalusky, A. S.; Olayo-Valles, R.; Taylor, C. J.; Hillmyer, M. A. Mesoporous Polystyrene Monoliths. *J. Am. Chem. Soc.* **2001**, *123*, 1519−1520.
(46) Zalusky, A. S.; Olayo-Valles, R.; Wolf, J. H.; Hillmyer, M. A. Ordered Nanoporous Polymers from Polystyrene-polylactide Block Copolymers. *J. Am. Chem. Soc.* **2002**, *124*, 12761−12773.
(47) Ho, R. M.; Tseng, W. H.; Fan, H. W.; Chiang, Y. W.; Lin, C. C.; Ko, B. T.; Huang, B. H. Solvent-induced Microdomain Orientation in Polystyrene-*b*-poly(L-lactide) Diblock Copolymer Thin Films for Nanopatterning. *Polymer* **2005**, *46*, 9362−9377.
(48) Uehara, H.; Yoshida, T.; Kakiage, M.; Yamanobe, T.; Komoto, T.; Nomura, K.; Nakajima, K.; Matsuda, M. Nanoporous Polyethylene Film Prepared from Bicontinuous Crystalline/Amorphous Structure of Block Copolymer Precursor. *Macromolecules* **2006**, *39*, 3971−3974.

DOI: 10.1021/acs.macromol.6b01725
Macromolecules XXXX, XXX, XXX−XXX

(49) Uehara, H.; Kakiage, M.; Sekiya, M.; Sakuma, D.; Yamonobe, T.; Takano, N.; Barraud, A.; Meurville, E.; Ryser, P. Size-Selective Diffusion in Nanoporous but Flexible Membranes for Glucose Sensors. *ACS Nano* **2009**, *3*, 924−932.
(50) Pitet, L. M.; Amendt, M. A.; Hillmyer, M. A. Nanoporous Linear Polyethylene from a Block Polymer Precursor. *J. Am. Chem. Soc.* **2010**, *132*, 8230−8231.
(51) Hsiao, T. J.; Lee, J. Y.; Mao, Y. C.; Chen, Y. C.; Tsai, J. C.; Lin, S. C.; Ho, R. M. Stereoregular Diblock Copolymers of Syndiotactic Polystyrene Derivatives and Polylactide: Syntheses and Self-Assembled Nanostructures. *Macromolecules* **2010**, *44*, 286−298.
(52) Jeng, U. S.; Su, C. H.; Su, C. J.; Liao, K. F.; Chuang, W. T.; Lai, Y. H.; Chang, J. W.; Chen, Y. J.; Huang, Y. S.; Lee, M. T.; Yu, K. L.; Lin, J. M.; Liu, D. G.; Chang, C. F.; Liu, C. Y.; Chang, C. H.; Liang, K. S. A Small/Wide-Angle X-ray Scattering Instrument for Structural Characterization of Air−Liquid Interfaces, Thin Films and Bulk Specimens. *J. Appl. Crystallogr.* **2010**, *43*, 110−121.
(53) Strobl, G. R.; Schneider, M. Direct Evaluation of the Electron Density Correlation Function of Partially Crystalline Polymers. *J. Polym. Sci., Polym. Phys. Ed.* **1980**, *18*, 1343−1359.
(54) Roe, R. *Methods of X-ray and Neutron Scattering in Polymer Science*; Oxford University Press: New York, 2000; p 201.
(55) Ishihara, N.; Kuramoto, M.; Uoi, M. Stereospecific Polymerization of Styrene Giving the Syndiotactic Polymer. *Macromolecules* **1988**, *21*, 3356−3360.
(56) Sakai, F.; Nishikawa, K.; Inoue, Y.; Yazawa, K. Nucleation Enhancement Effect in Poly(L-lactide) (PLLA)/Poly(ϵ-caprolactone) (PCL) Blend Induced by Locally Activated Chain Mobility Resulting from Limited Miscibility. *Macromolecules* **2009**, *42*, 8335−8342.
(57) Brandrup, J.; Immergut, E. H.; Grulke, E. A. *Polymer Handbook*; Wiley: New York, 1999.
(58) Blomqvist, J.; Mannfors, B.; Pietilä, L.-O. Amorphous Cell Studies of Polyglycolic, Poly(L-lactic), Poly(L,D-lactic) and Poly(glycolic/L-lactic) Acids. *Polymer* **2002**, *43*, 4571−4583.
(59) Chen, H. L.; Hsiao, S. C.; Lin, T. L.; Yamauchi, K.; Hasegawa, H.; Hashimoto, T. Microdomain-Tailored Crystallization Kinetics of Block Copolymers. *Macromolecules* **2001**, *34*, 671−674.
(60) Chung, T. M.; Wang, T. C.; Ho, R. M.; Sun, Y. S.; Ko, B. T. Polymeric Crystallization under Nanoscale 2D Spatial Confinement. *Macromolecules* **2010**, *43*, 6237−6240.
(61) Esposito, G.; Tarallo, O.; Petraccone, V. Crystal Structure of Form I of Syndiotactic Poly(*para*-methylstyrene). *Macromolecules* **2006**, *39*, 5037−5042.
(62) De Rosa, C.; Petraccone, V.; Dal Poggetto, F.; Guerra, G.; Pirozzi, B.; Di Lorenzo, M. L.; Corradini, P. Crystal Structure of Form III of Syndiotactic Poly(*p*-methylstyrene). *Macromolecules* **1995**, *28*, 5507−5511.
(63) Iuliano, M.; Guerra, G.; Petraccone, V.; Corradini, P.; Pellecchia, C. Polymorphism of Syndiotactic Poly (*p*-methylstyrene) Unoriented Samples. *New Polym. Mater.* **1992**, *3*, 133−144.
(64) Cartier, L.; Okihara, T.; Ikada, Y.; Tsuji, H.; Puiggali, J.; Lotz, B. Epitaxial Crystallization and Crystalline Polymorphism of Polylactides. *Polymer* **2000**, *41*, 8909−8919.
(65) Zhang, J.; Tashiro, K.; Tsuji, H.; Domb, A. J. Disorder-to-order Phase Transition and Multiple Melting Behavior of Poly(L-lactide) Investigated by Simultaneous Measurements of WAXD and DSC. *Macromolecules* **2008**, *41*, 1352−1357.

DOI: 10.1021/acs.macromol.6b01725
Macromolecules XXXX, XXX, XXX−XXX